The Astrophysical Journal, 929:140 (14pp), 2022 April 20 https://doi.org/10.3847/1538-4357/ac5d57

An Empirical Representation of a Physical Model for the ISM [C II], CO, and [C I] Emission at Redshift $1 \leqslant z \leqslant 9$

Shengqi Yang[1,2], Gergö Popping[3], Rachel S. Somerville[4], Anthony R. Pullen[2,4], Patrick C. Breysse[2,4], and Abhishek S. Maniyar[2]
[1] Carnegie Observatories, 813 Santa Barbara Street, Pasadena, CA 91101, USA; syang@carnegiescience.edu
[2] Center for Cosmology and Particle Physics, Department of Physics, New York University, 726 Broadway, New York, NY 10003, USA
[3] European Southern Observatory, Karl-Schwarzschild-Strasse 2, D-85748, Garching, Germany
[4] Center for Computational Astrophysics, Flatiron Institute, New York, NY 10010, USA
Received 2021 August 17; revised 2022 March 4; accepted 2022 March 10; published 2022 April 21

Abstract

Submillimeter emission lines produced by the interstellar medium (ISM) are strong tracers of star formation and are some of the main targets of line intensity mapping (LIM) surveys. In this work we present an empirical multiline emission model that simultaneously covers the mean, scatter, and correlations of [C II], CO $J = 1$–0 to $J = 5$–4, and [C I] lines in the redshift range $1 \leqslant z \leqslant 9$. We assume that the galaxy ISM line emission luminosity versus halo mass relations can be described by double power laws with redshift-dependent lognormal scatter. The model parameters are then derived by fitting to the state-of-the-art semianalytic simulation results that have successfully reproduced multiple submillimeter line observations at $0 \leqslant z \lesssim 6$. We cross-check the line emission statistics predicted by the semianalytic simulation and our empirical model, finding that at $z \geqslant 1$ our model reproduces the simulated line intensities with fractional error less than about 10%. The fractional difference is less than 25% for the power spectra. Grounded on physically motivated and self-consistent galaxy simulations, this computationally efficient model will be helpful in forecasting ISM emission-line statistics for upcoming LIM surveys.

Unified Astronomy Thesaurus concepts: Intergalactic medium (813); Diffuse radiation (383); Large-scale structure of the universe (902)

1. Introduction

Two cosmic epochs that are of great interest for modern astrophysics are the epoch of reionization at redshift $z > 6$ and the cosmic "high noon" era, when the cosmic star formation history peaked, at $z \sim 2$ (Madau & Dickinson 2014). Since the molecular clouds distributed throughout the interstellar medium (ISM) host star formation, and the star-forming activity in return influences the nearby ISM environment, ISM emission lines are unique tracers for the physical properties of the stellar population and the star-forming environment. Among various molecular and fine-structure lines, radiations with wavelengths between 15 μm and 1 mm, also referred to as submillimeter emission lines, are particularly promising for observation since they can penetrate dense molecular clouds. Some of the popular submillimeter observational targets are the molecular ISM tracers, including the CO rotational transitions, and [C I] fine-structure lines; tracers of photodissociation regions such as the [C II] 157 μm line, which is also the brightest far-infrared line; and tracers of H II regions, including the [O III] 88 μm and 52 μm fine-structure lines and [N II] 122 μm and 205 μm transitions.

Our observational view of submillimeter emission-line properties of galaxies in the nearby and distant universe has exploded since the launch of the Herschel Space Observatory and the commissioning of the Atacama Large Millimeter Array (ALMA) in 2010. However, there is concern about whether the bright sources observable by those instruments are representative of the general galaxy population. An emerging observational technique referred to as line intensity mapping (LIM; Kovetz et al. 2017) is designed to complement traditional galaxy surveys. Instead of resolving individual targets with high spatial resolution, LIM measures the aggregated emission along the line of sight with high spectral resolution, including radiation contributed by faint galaxies. LIM is therefore more suitable for probing the average galaxy properties during the cosmic epochs of interest. However, since the beam sizes of LIM surveys are generally much larger than the target sizes, confusion is a major challenge for LIM survey data analysis (Helou & Beichman 1990).

Up to now, LIM surveys have achieved preliminary [C II] and CO detections at high redshift (Keating et al. 2016, 2020; Pullen et al. 2018; Yang et al. 2019), and more surveys with higher spectral resolution are planned in the upcoming decade to further confirm or extend those detections. Motivated by the prospects of these upcoming experiments, reliable submillimeter line emission models are needed to provide theoretical predictions for the observational interpretation and forecasts. Ideally, such a submillimeter model framework should connect the line emission observables to the physical properties of the ISM gas clouds, galaxies, and dark matter halos. It should also simultaneously predict as many emission lines as possible to provide a comprehensive understanding of the multiphase ISM environment. It is difficult to construct such an analytic model because the microphysical processes involved in different submillimeter line emissions vary case by case. Moreover, it is challenging to connect line emission mechanisms happening on the atomic scale to the sub-parsec-scale molecular clouds, kiloparsec-scale galaxies, and megaparsec-scale dark matter halos. There are many analytic models in the literature describing the major submillimeter LIM targets, including CO, [C II], [O III], and [N II] lines (e.g., Lidz et al. 2011; Gong

et al. 2012; Pullen et al. 2013; Kamenetzky et al. 2014; Silva et al. 2015; Mashian et al. 2015; Li et al. 2016; Pullen et al. 2018; Padmanabhan 2019; Sun et al. 2019; Yang & Lidz 2020; Padmanabhan et al. 2021). All those models include empirical treatments to some degree and fail to simultaneously cover all the lines of interest. In particular, there is a lack of models that predict the CO rotational transitions with high J quantum states, which are the major low-redshift interlopers for many LIM surveys.

An alternative approach is to combine numerical hydrodynamic galaxy formation simulations with radiative transfer, photoionization, and photodissociation region modeling (e.g., Olsen et al. 2017; Moriwaki et al. 2018; Leung et al. 2020; Olsen et al. 2021). The strength of the numerical simulation approach is that detailed properties of the gas distribution, temperature, and radiation field can be obtained down to the resolution of the simulation. However, all simulations that cover cosmological volumes have resolution considerably coarser than the molecular cloud scales relevant for line emission, so a "subgrid" model must be applied on top of the simulation as part of the line emission model. Due to the rather high computational expense of this approach, it is currently not feasible to produce predictions for large numbers of galaxies (state of the art is $<$700 galaxies) or to explore uncertainties in the subgrid recipes for physical processes in the simulations or in the line emission modeling interface. In addition, portability of the numerical approach can be limited since many simulations are not open source.

A "middle way" is provided by coupling semianalytic models of galaxy formation with a submillimeter line emission modeling framework (Popping et al. 2014a, 2016, 2019; Lagache et al. 2018). The state-of-the-art submillimeter line simulation framework is introduced in Popping et al. (2019, hereafter P19) and Yang et al. (2021). This framework combines the semianalytic galaxy formation model (SAM) developed by the "Santa Cruz" group (Somerville & Primack 1999; Somerville et al. 2008b, 2012; Porter et al. 2014; Popping et al. 2014b; Somerville et al. 2015) with a subgrid model for molecular cloud properties and the DESPOTIC (Krumholz 2014) spectral synthesis tool. The SAM provides information on the global properties (gas mass, metallicity, density) for up to millions of galaxies over a very wide range in halo mass and redshift, and precomputed tables from DESPOTIC provide the calculations of the thermochemical evolution and emergent line emission from optically thick clouds. The models include physics-grounded treatments for ISM multiphase partitioning, molecular cloud distribution, and cloud density profile variation. The full pipeline is many orders of magnitude faster than a fully numerical approach and yields results that are broadly consistent (e.g., Leung et al. 2020). The P19 submillimeter SAM framework has successfully reproduced the observed strength of [C II] 157 μm fine-structure lines, multiple CO rotational transitions, and [C I] fine-structure emissions at $0 \leqslant z \lesssim 6$.

Motivated by the need for a physically grounded multiline analytic model, in this work we present an empirical model for [C II], CO, and [C I] line luminosity as a function of halo mass, calibrated to accurately reproduce the updated P19 submillimeter SAM results. We assume that the line intensity L versus halo mass M relations follow a double power-law trend, together with a redshift-dependent lognormal scatter. We then study the evolution of $L(M)$ relations and their scatter and correlations over the redshift range $0 < z \leqslant 9$. As a first application, we use this model to predict the line intensities and power spectra, finding that our empirical model yields results that match the direct SAM simulation results with fractional error better than 25% at $1 \leqslant z \leqslant 9$. Given that CO rotational transitions and [C I] fine-structure lines are potentially important low-redshift interlopers for many [C II] LIM surveys, this model will be useful for testing the signal detectability and interloper line removal techniques for upcoming LIM surveys (e.g., Breysse et al. 2021; A. Pullen et al. 2022, in preparation).

We emphasize that the Santa Cruz SAM contains numerous simplifying assumptions, and there are many uncertainties in the physical processes, particularly those connected to stellar and AGN feedback. This is the case for all existing a priori models of galaxy formation, whether semianalytic or numerical (e.g., Somerville & Davé 2015). The model assumptions are based on phenomenology or results from numerical simulations, and the fiducial model parameters have been chosen to produce predictions that are consistent with a broad range of observations of galaxy properties, as documented in an extensive literature stretching over several decades (see Section 2). Similarly, there are also uncertainties and assumptions that affect the predictions of the P19 submillimeter SAM model (which have been rather extensively documented in that work). We do not mean to suggest that these models are the definitive "right answer"—instead, our goal is to introduce a framework for efficiently translating the predictions from physically motivated models into LIM observables. This framework is quite general and should be extensible to nearly any physics-based model or to variations in the model physics modules and parameters.

The plan of this paper is as follows: We introduce the Santa Cruz SAM for galaxy formation in Section 2. In Section 3 we review the DESPOTIC-based submillimeter model proposed by P19 for estimating the submillimeter line luminosities of the simulated galaxies, and we describe the model refinement made in this work. We introduce the empirical $L(M)$ relations and the model calibration processes in Section 4. The SAM model line statistics comparisons are presented in Section 5. We conclude in Section 6. Throughout this work we adopt a flat ΛCDM cosmology and assume cosmological parameters $\Omega_m = 0.308$, $\Omega_\Lambda = 0.692$, $h = H_0/(100\,\mathrm{km\,s^{-1}\,Mpc^{-1}}) = 0.678$, $\sigma_8 = 0.831$, and $n_s = 0.9665$ (Planck Collaboration et al. 2016). We adopt a baryonic fraction of $f_b = 0.1578$ and a Chabrier initial mass function (Chabrier 2003).

2. Santa Cruz Semianalytic Model

In this work we use the SAM developed by the "Santa Cruz" group to generate galaxy samples. The development of this SAM framework is introduced in detail in a series of papers (Somerville & Primack 1999; Somerville et al. 2008b, 2012; Popping et al. 2014b; Porter et al. 2014; Somerville et al. 2015). We will only introduce the key features in this section, and we refer our readers to Somerville et al. (2008b, 2015) for more details.

Instead of solving the equations of gravity, hydrodynamics, and thermodynamics for particles or grid cells, SAMs adopt physically motivated treatments of the bulk flows of mass and metals between different "reservoirs" (e.g., the diffuse intergalactic medium outside of resolved halos, hot diffuse halo gas, cold dense ISM gas, stars), set within the framework of dark

matter halo formation predicted by ΛCDM and encapsulated in the form of "merger trees."

First, we divide the dark matter halo mass range that we consider in this work ($10 \leqslant \log(M_{\rm halo}/[M_\odot]) \leqslant 13$)[5] into 100 log mass bins and generate 100 dark matter halos in each bin. This halo mass range is selected because halos with mass greater than 10^{13} $M_\odot$ are very rare objects, while the SAM predicts that halos less massive than 10^{10} $M_\odot$ are too faint to significantly influence the submillimeter line emission statistics (see Yang et al. 2021, Appendix A for a more detailed discussion). The SAM then estimates the merging history of each halo using a method based on the extended Press −Schechter formalism (Somerville & Kolatt 1999; Somerville et al. 2008b). The halo merger tree is evolved back in time until the progenitors are less massive than 1% of the root halo or 10^8 $M_\odot$, whichever is smaller. Before cosmic reionization, each halo is assigned hot gas with mass determined by the product of the universal baryonic fraction and the halo virial mass. After reionization, the mass filtering scale associated with UV photoionization heating by the metagalactic background from hydrodynamic simulations (Okamoto et al. 2008) is used to determine the fraction of gas that is accreted as a function of halo mass and redshift.

The SAM computes the rate that gas cools and accretes into the ISM using a spherically symmetric standard cooling model as described in Somerville et al. (2008b). Gas is assumed to initially form a disk with an exponential radial density profile, and the disk size is estimated following Somerville et al. (2008a). The cold gas surface density profile is used along with the gas metallicity and the local UV radiation field (assumed proportional to the SFR) to estimate the fraction of ionized, atomic, and molecular gas in each annulus as a function of radius within each disk, using a prescription based on numerical hydrodynamic simulations (Somerville et al. 2015). The new SFR is then computed based on the surface density of molecular gas, motivated by observations. This feature makes Santa Cruz SAM particularly suitable for ISM line emission predictions. The SFR, stellar mass, cold gas mass, and other predictions of the Santa Cruz SAM have been shown to be broadly consistent with observations from the local universe to $z \sim 10$ (Popping et al. 2014b; Somerville et al. 2015; Yung et al. 2019a, 2019b, 2020a, 2020b; Somerville et al. 2021).

3. Submillimeter Emission-line Modeling

In this work we adopt the submillimeter line emission modeling framework proposed by P19 (hereafter submillimeter SAM), which adds a subgrid model for molecular cloud properties to the Santa Cruz SAM and couples this cloud population to the DESPOTIC code. As mentioned in the introduction, one major challenge of applying submillimeter line emission models to cosmological simulations is building connections between physical processes happening at atomic scales, molecular cloud scales, and the scales of galaxies. P19 developed a subgrid approach to address this problem. Specifically, each galaxy simulated by the SAM is divided into multiple radial annuli. In each ISM annulus, the masses of the molecular cloud population are assigned by selecting randomly from a power-law mass distribution with parameters that depend on the mean density in the annulus. The molecular clouds are all assumed to be spherically symmetric and are assigned a radial density profile. The [C II], CO, and [C I] luminosities of each molecular cloud are then estimated through the following process: First, multiple grid points are selected in the five-dimensional parameter space, including cloud mass, gas pressure, metallicity, external-ultraviolet and cosmic-ray radiation field strength, and the redshift $\{M_{\rm cloud}, P_{\rm ext}, Z, F_{\rm ext}, z\}$. To ensure convergence of the numerical solutions, each molecular cloud is further divided into 25 regions so that the gas property within each region is close to constant. This set of physical properties is then input to DESPOTIC, which uses a one-zone model to compute the dominant heating, cooling, and chemical processes. These include grain photoelectric heating, heating of the dust by infrared and ultraviolet radiation, thermal cooling of the dust, cosmic-ray and X-ray heating, collisional energy exchange between dust and gas, and a simple network for carbon chemistry. The numerical solutions provided by DESPOTIC are used to create a lookup table, which allows a mapping from a set of physical properties to [C II], CO, and [C I] line luminosity. Finally, the relevant submillimeter line luminosities of each simulated galaxy are estimated by summing up the radiation from all the molecular clouds within it.

The submillimeter SAM line luminosity simulation results are somewhat sensitive to the assumed cloud radial density profile. P19 have shown that models with a Plummer density profile reproduce various [C II], CO, and [C I] line observations at redshift $0 \leqslant z \lesssim 6$. However, several subsequent works have shown that the submillimeter SAM underestimates [C II] and [C I] luminosities compared to more recent ALMA detections at high redshift (e.g., Béthermin et al. 2020; Valentino et al. 2020). To resolve the tension between the submillimeter SAM predictions and recent observations, in this work we assume a power-law radial density profile for each molecular cloud, as first suggested by Yang et al. (2021). This change of the cloud density profile does not significantly influence the CO luminosity predictions, but it effectively increases the [C II] and [C I] line strengths at high redshift such that the model predictions are consistent with observations. We also created a finer grid in parameter space for the DESPOTIC lookup table calculation to ensure accurate linear interpolations. We randomly select 115,000 test points in the five-dimensional parameter space $\{10^4 < M_{\rm cloud}/[M_\odot] < 10^7, 10^3 < P_{\rm ext}/k_{\rm B}/10^4[{\rm cm^{-3}K}] < 10^9, 10^{-3} < Z/[Z_\odot] < 10^{0.5}, 10^{-3} < F_{\rm ext}/[{\rm Habing}] < 10^4, 0 < z < 9\}$ and find that more than 78.5% of the [C II], CO, and [C I] linear interpolations given by the lookup table agree with the DESPOTIC numerical solutions with better than 20% fractional error.

4. An Empirical [C II], CO, and [C I] Model Calibrated to the Submillimeter SAM

In order to represent the submillimeter SAM simulation results in a more computationally efficient and portable way, in this section we introduce an empirical model that captures the average, dispersion, and correlation of line luminosities versus halo mass relations $L(M)$ simulated following the framework introduced in Sections 2 and 3. This model reproduces SAM line intensities and power spectra with better than 25% fractional error at $z \geqslant 1$. The SAM model power spectra fractional difference further reduces to less than 15% at $z \geqslant 3$. For applications that require more accurate submillimeter line simulations, in particular at redshift $z < 1$, we provide tables of

[5] In this work we use log to denote a base-10 logarithm, while ln denotes a natural logarithm.

the submillimeter SAM $L(M)$ simulation results at https://users.flatironinstitute.org/~rsomerville/Data_Release/LIM/.

In this work we define the submillimeter line luminosity of each dark matter halo as the sum of the luminosity of all galaxies within the halo, and we treat halos as the smallest submillimeter line emitters. The $L(M)$ model therefore cannot capture the submillimeter line fluctuations on scales smaller than the size of the halo. Since the beam sizes of LIM surveys are generally large, such a model is still suitable for making many LIM forecasts. We leave a more careful treatment of the "one-halo term" (which would require separate modeling of central and satellite galaxies, along with their location within the halo), which is crucial for galaxy spectroscopic survey forecasts, to future works.

4.1. The Average L(M) Model

The main observables of LIM surveys, including the intensity of line emission and the two-halo term of the auto-power spectrum, can be estimated through a combination of the average line luminosity versus halo mass $L(M)$ model and a halo model, which provides the number density and bias of halos as a function of their mass and redshift. The $L(M)$ relations and their redshift evolution have been studied via many different approaches in the literature. Although upcoming LIM surveys that cover large cosmic volumes and capture radiation of faint emitters will result in stronger constraints on the $L(M)$ relations, the slopes of $L(M)$ relations at very high and low halo mass are currently poorly determined owing to a lack of observational data for very massive halos with $M \gtrsim 10^{12}[M_\odot]$ and very faint sources with $M \lesssim 10^{11}[M_\odot]$. As a result, current empirical $L(M)$ models in the literature range from linear to power-law relations (e.g., Lidz et al. 2011; Pullen et al. 2013; Padmanabhan 2019). In this work we assume a double power-law $L(M)$ relation as suggested by Padmanabhan (2018):

$$\frac{L}{[L_\odot]} = 2N\frac{M}{[M_\odot]}\left[\left(\frac{M/[M_\odot]}{M_1}\right)^{-\alpha} + \left(\frac{M/[M_\odot]}{M_1}\right)^{\beta}\right]^{-1}, \quad (1)$$

where the four free parameters M_1, N, α, and β control the mass of the turnover, amplitude, slope at $M/[M_\odot] < M_1$, and slope at $M/[M_\odot] > M_1$ for the $L(M)$ relation. A schematic diagram of how $\{M_1, N, \alpha, \beta\}$ control the shape of the $L(M)$ model is presented in Figure 1. A double power-law relation has frequently been used in the literature to describe galaxy–dark matter connections, including stellar mass or luminosity versus halo mass relations (Yang et al. 2012; Moster et al. 2013). Stellar mass–halo mass empirical models that are consistent with observational constraints (e.g., Behroozi et al. 2010, 2013, 2019) indicate that the halo star formation efficiency increases with halo mass from $M \sim 10^{10}\ M_\odot$ to a redshift-dependent threshold M_1. For more massive halos, the star formation efficiency decreases with halo mass instead, leading to a shallower SFR–M slope. Massive star/supernova (SN) feedback drives the slope of the galaxy–halo relation at masses below M_1, and active galactic nucleus (AGN) feedback is the main driver at higher halo masses. Specifically, stellar feedback depletes the cold gas reservoir of low-mass halos via strong outflows, which are less efficient at removing gas in more massive halos with deeper potential wells. On the other hand, massive halos are more likely to harbor massive bulge-dominated galaxies, which host supermassive black holes. These black holes drive AGN feedback in the form of radiation-pressure-driven winds, which can remove cold gas from the galaxy, and powerful jets, which can heat the hot gas in the halo and suppress or quench cooling. As a result, the dependence of the efficiency of stellar-driven winds on galaxy circular velocity is expected to determine the slope of the double power law at $M < M_1$ (α), the efficiency of the jet mode AGN feedback coupling with the hot gas is expected to determine the slope at $M > M_1$, and the relative importance of these two feedback channels determines where they cross, which determines the value of M_1. Since the ISM submillimeter lines considered in this work all trace relatively dense star-forming gas, the line luminosities are strongly correlated to SFR. It is therefore natural to expect the average $L(M, z)$ relations to follow similar trends.

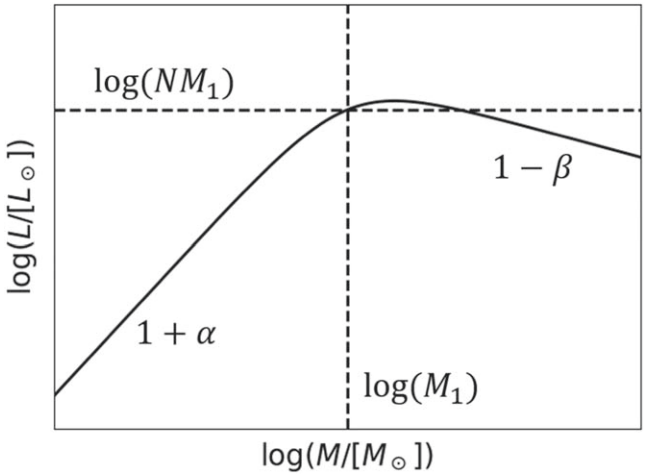

Figure 1. Sketch of the double power-law $L(M)$ relation characterized by parameters $\{M_1, N, \alpha, \beta\}$ introduced in Equation (1). M_1 controls the mass of the turnover of the $L(M)$ relation, N characterizes its amplitude, and α and β control the slopes of the $L(M)$ relation at halo mass range $M/[M_\odot] < M_1$ and $M/[M_\odot] > M_1$, respectively. Adapted from Moster et al. (2013).

In each of the 91 redshift slices uniformly distributed in $0 \leqslant z \leqslant 9$, we divide 10^4 halos simulated by the submillimeter SAM into 30 mass bins. The submillimeter line luminosity of each halo is determined by the total luminosity of all the galaxies within the halo. We then select star-forming halos whose central galaxy satisfies $\mathrm{sSFR} > 1/(3t_H(z))$ to calculate the average $L(M)$ relation. Here sSFR is the specific star formation rate defined as the ratio between the galaxy SFR and stellar mass, and $t_H(z)$ is the Hubble time at the halo redshift. We then fit for the values of the parameters in Equation (1) using the tabulated $L(M)$ relations from the submillimeter SAM through a nonlinear least-squares approach. We find that the average $L(M)$ statistic predicted by the submillimeter SAM is well represented by the double power-law relation. The redshift evolution of the parameters $\{M_1, N, \alpha, \beta\}$ is summarized in Table 1. In order to describe the redshift evolution of the double power-law model parameters with simple functions, we bin the results into coarser redshift bins $1 \leqslant z < 4$, $4 \leqslant z < 5$, $5 \leqslant z \leqslant 9$ and model the parameter redshift dependence separately. As one example, in Figure 2 we show the comparison between $\{M_1, N, \alpha, \beta\}$ best-fit values (blue points)

Table 1
Redshift Evolution of Parameters in the $L(M)$ Double Power-law Model Equation (1)

Line	$\log M_1$	$\log N$	α	β
		$1.0 \leqslant z < 4.0$		
C II	$12.11z^{-0.04105}$	$-0.907\exp(-z/0.867) - 3.04$	$1.35 + 0.450z - 0.0805z^2$	$2.57\exp(-z/1.55) + 0.0575$
CO $J = 1$–0	$12.13 - 0.1678z$	$-6.855 + 0.2366z - 0.05013z^2$	$1.642 + 0.1663z - 0.03238z^2$	$1.77\exp(-z/2.72) - 0.0827$
CO $J = 2$–1	$12.12 - 0.1704z$	$-5.95 + 0.278z - 0.0521z^2$	$1.69 + 0.126z - 0.0280z^2$	$1.80\exp(-z/2.76) - 0.0678$
CO $J = 3$–2	$12.1 - 0.171z$	$-5.53 + 0.329z - 0.0570z^2$	$1.843 + 0.08405z - 0.02485z^2$	$1.88\exp(-z/2.74) - 0.0623$
CO $J = 4$–3	$12.09 - 0.1662z$	$-5.35 + 0.404z - 0.0657z^2$	$2.24 - 0.0891z$	$2.017\exp(-z/2.870) - 0.1127$
CO $J = 5$–4	$12.12 - 0.1796z$	$-5.37 + 0.515z - 0.0802z^2$	$2.14 + 0.110z - 0.0371z^2$	$2.39\exp(-z/2.55) - 0.0890$
CI $J = 1$–0	$1.026\exp(-z/2.346) + 11.20$	$-1.451\exp(-z/1.893) - 5.046$	$-0.741\exp(-z/0.739) + 1.86$	$1.26 - 0.198z$
CI $J = 2$–1	$1.135\exp(-z/2.616) + 11.13$	$-2.03\exp(-z/1.80) - 4.44$	$-1.16\exp(-z/0.706) + 2.00$	$1.54 - 0.259z$
		$4.0 \leqslant z < 5.0$		
C II	$8.69 + 1.26z - 0.143z^2$	$-5.467 + 1.056z - 0.1133z^2$	$6.135 - 1.786z + 0.1837z^2$	$0.443 - 0.0521z$
CO $J = 1$–0	$11.75 - 0.06833z$	$-6.554 - 0.03725z$	$3.73 - 0.833z + 0.0884z^2$	$0.598 - 0.0710z$
CO $J = 2$–1	$11.74 - 0.07050z$	$-5.57 - 0.0250z$	$4.557 - 1.215z + 0.1300z^2$	$0.657 - 0.0794z$
CO $J = 3$–2	$11.74 - 0.07228z$	$-5.06 - 0.0150z$	$5.253 - 1.502z + 0.1609z^2$	$0.707 - 0.0879z$
CO $J = 4$–3	$11.73 - 0.07457z$	-4.784	$5.74 - 1.67z + 0.178z^2$	$0.762 - 0.0984z$
CO $J = 5$–4	$11.73 - 0.07798z$	$-3.81 - 0.359z + 0.0419z^2$	$6.12 - 1.77z + 0.188z^2$	$0.846 - 0.115z$
CI $J = 1$–0	$8.54 + 1.33z - 0.157z^2$	$-6.96 + 0.750z - 0.0807z^2$	$8.42 - 2.91z + 0.320z^2$	$0.837 - 0.103z$
CI $J = 2$–1	$8.823 + 1.206z - 0.1445z^2$	$-4.906 + 0.05632z$	$9.275 - 3.225z + 0.3543z^2$	$0.94 - 0.12z$
		$z \geqslant 5$		
C II	$11.92 - 0.1068z$	$-2.37 - 0.130z$	$2.82 - 0.298z + 0.0196z^2$	$1760\exp(-z/0.520) + 0.0782$
CO $J = 1$–0	$11.63 - 0.04943z$	$-6.274 - 0.09087z$	$2.56 - 0.223z + 0.0142z^2$	$33.4\exp(-z/0.846) + 0.160$
CO $J = 2$–1	$11.63 - 0.05266z$	$-5.26 - 0.0849z$	$2.47 - 0.210z + 0.0132z^2$	$38.3\exp(-z/0.841) + 0.169$
CO $J = 3$–2	$11.62 - 0.0550z$	$-4.72 - 0.0808z$	$2.53 - 0.220z + 0.0139z^2$	$31.5\exp(-z/0.879) + 0.170$
CO $J = 4$–3	$11.6 - 0.0529z$	$-4.40 - 0.0744z$	$2.59 - 0.206z + 0.0120z^2$	$41.6\exp(-z/0.843) + 0.172$
CO $J = 5$–4	$11.58 - 0.05359z$	$-4.21 - 0.0674z$	$2.87 - 0.257z + 0.0157z^2$	$21.8\exp(-z/0.957) + 0.168$
CI $J = 1$–0	$4.294\exp(-z/2.479) + 10.68$	$1.89\exp(-z/5.73) - 6.03$	$1.04 + 0.165z$	$2090\exp(-z/0.520) + 0.204$
CI $J = 2$–1	$4.37\exp(-z/2.38) + 10.7$	$1.48\exp(-z/6.14) - 5.31$	$1.17 + 0.169z$	$3960\exp(-z/0.487) + 0.221$

and our model summarized in Table 1 (red curves) for the CO $J = 1$–0 line.

We find that in the redshift range $1 \leqslant z \leqslant 9$ the characteristic halo mass M_1 that corresponds to the star formation efficiency peak decreases from 10^{12} to 10^{11} $M_\odot$, in agreement with Behroozi et al. (2013). The parameter N that controls the overall amplitude of $L(M, z)$ peaks at $z \sim 2$, consistent with the observed cosmic star formation rate density redshift evolution. The parameter α that controls the $L(M)$ slope on the $M < M_1$ side shows a relatively weak redshift dependence. This is because the slope of the dependence of the mass loading of stellar-driven winds on galaxy circular velocity is assumed to be a fixed value in these models. There is a weak dependence on redshift due to the weakly evolving relationship between halo mass and galaxy circular velocity. The parameter β that characterizes the $L(M)$ relation slope on the high halo mass end increases much more significantly from $z \sim 6$ to $z = 1$, indicating that, on average, the star formation activity within massive halos becomes less efficient as time goes by. This is because in the SC SAM black hole growth is tied to bulge growth, and massive bulges build up at late times via gas-poor mergers. The radio jet power is assumed to be proportional to the black hole mass, motivated by observations (Somerville et al. 2008b). As the black hole mass increases over time, the gas heating rate due to these jets can approach or exceed the cooling rate in massive halos, leading to quenching of star formation and a decrease of the $L(M)$ slope on the high-mass end.

We present example comparisons between $L(M)$ relations from the submillimeter SAM and our empirical model for [C II], CO $J = 1$–0 to $J = 5$–4, and [C I] $J = 1$–0 to $J = 2$–1 lines in Figure 3, with fractional differences $(L_{\rm SAM} - L_{\rm model})/L_{\rm SAM}$ specified in the inset of each panel. Our double power-law $L(M, z)$ model generally recovers the submillimeter SAM predictions with better than 20% accuracy, but the fractional difference can be large at low halo mass. Since halos with $M \leqslant 10^{11}$ $M_\odot$ are very faint submillimeter line emission sources, we will show in Section 5 that the inaccuracy of our $L(M)$ model at $M \leqslant 10^{11}$ $M_\odot$ does not corrupt its LIM summary statistics predictions.

4.2. Halo Duty Cycle Factor

As mentioned in Section 4.1, we have removed quenched dark matter halos that are not forming stars rapidly and therefore are not likely to be luminous in [C II], CO, and [C I] lines from the $L(M)$ model fitting, so another important part of our empirical treatment is to model the fraction of star-forming halos $f_{\rm duty}$ in each halo mass bin and redshift slice. We calculate $f_{\rm duty}$ as the fraction of halos in each mass and redshift bin with a central galaxy that satisfies the condition $\mathrm{sSFR} > 1/(3t_{\rm H}(z))$, as introduced above:

$$f_{\rm duty}(M, z) = \frac{N_{\rm SF}(M, z)}{N_{\rm total}(M, z)}, \quad (2)$$

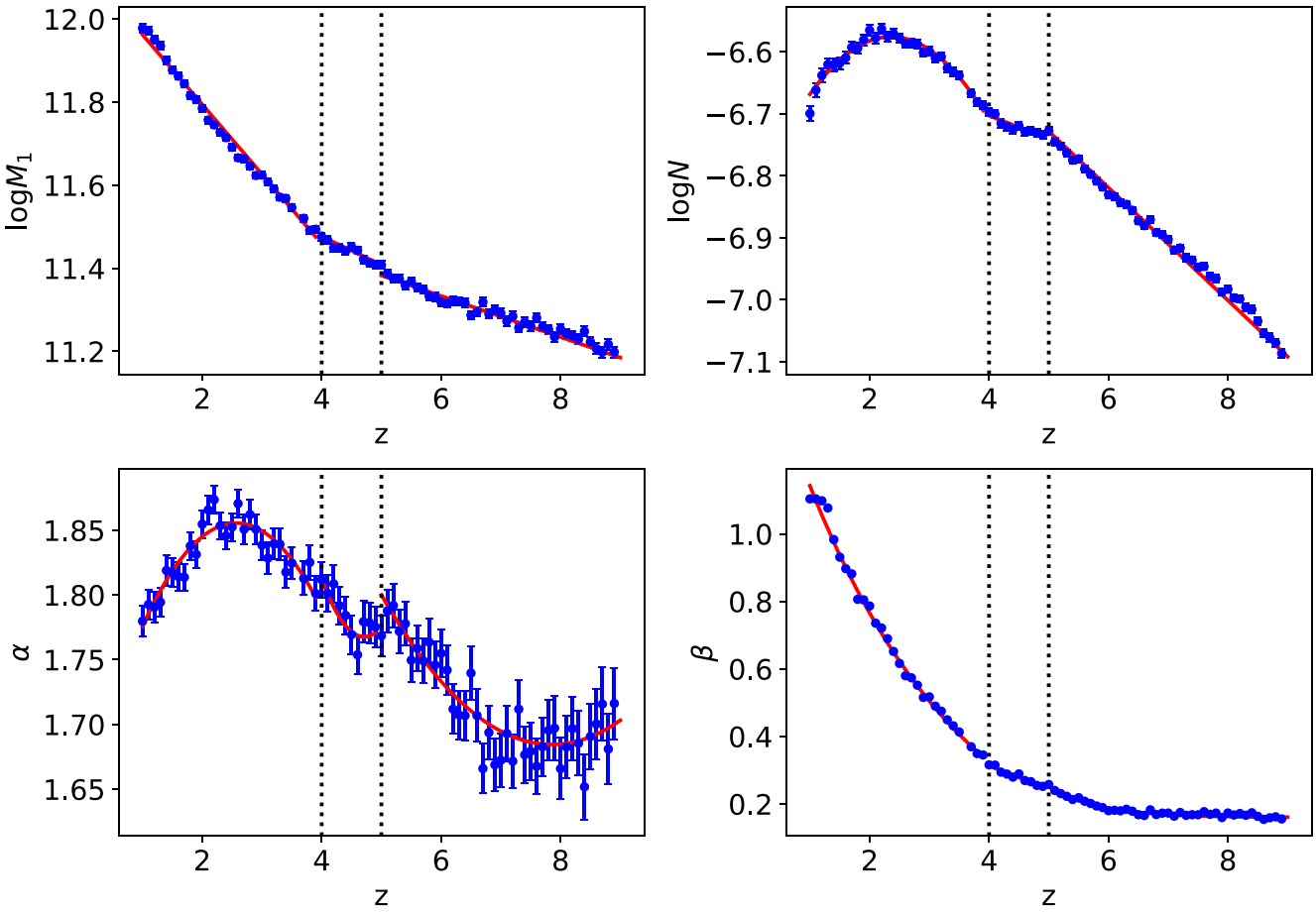

Figure 2. Redshift evolution of parameters $\{M_1, N, \alpha, \beta\}$ introduced in Equation (1) for CO $J = 1$–0. Blue points show the best-fit parameter values, while the red curves are our models summarized in Table 1.

where $N_{\rm SF}$ is the number of star-forming halos, while $N_{\rm total}$ is the total number of dark matter halos in the corresponding redshift and halo mass bin. We find that the $f_{\rm duty}(M)$ relation can be described by a double power law at redshift $1 \leqslant z < 4$:

$$f_{\rm duty} = \begin{cases} \dfrac{1}{1 + \left(\frac{M\,/\,[M_\odot]}{M_2}\right)^{\gamma}}, & \text{if } 1 \leqslant z < 4 \\ 1, & \text{if } 4 \leqslant z \leqslant 9 \end{cases} \quad (3)$$

with redshift evolution given by

$$\log M_2(z) = 11.73 + 0.6634z,$$
$$\gamma(z) = 1.37 - 0.190z + 0.0215z^2. \quad (4)$$

The gas accretion rate into halos decreases at $z < 1$ owing to the onset of the accelerating cosmic expansion. As a result, central galaxies living in less massive halos ($M \lesssim 10^{11}\ M_\odot$) start to become quenched by stellar feedback, causing a more complicated $f_{\rm duty}(M)$ behavior at low halo mass that cannot be fully captured by this simple double power-law relation. We show example comparisons between the $f_{\rm duty}(M)$ relations predicted by the submillimeter SAM and this model in Figure 4, with fractional difference $f_{\rm err} = (f_{\rm duty}^{\rm SAM} - f_{\rm duty}^{\rm model})/f_{\rm duty}^{\rm SAM}$ specified in the inset. The accuracy of our $f_{\rm duty}$ model is better than 20% in redshift range $1 \leqslant z \leqslant 9$ and halo mass range $10^{10}\ M_\odot \leqslant M \leqslant 10^{12.5}\ M_\odot$. The strong redshift dependence of $f_{\rm duty}$ at high halo masses is driven by the growth of massive black holes and the corresponding increase in the efficiency of AGN feedback, as described earlier.

4.3. L(M) Scatter and Multiline Correlations

With the average line luminosity versus halo mass $L(M)$ model and the halo duty cycle factor $f_{\rm duty}(M)$ model introduced in Sections 4.1 and 4.2, key LIM observables can be calculated quantitatively by combining these with halo models (e.g., Cooray & Sheth 2002; Schaan & White 2021). The intensities of [C II], CO, and [C I] lines can be estimated through

$$I_i(z) = \frac{c}{4\pi\nu_i^0 H(z)} \int dM \frac{dn}{dM} L_i(M, z) f_{\rm duty}\,, \quad (5)$$

where i is an index for submillimeter lines considered in this work, ν_i^0 is the rest-frame frequency of the target emission line, and dn/dM is the halo mass function. In this work we choose the Sheth & Tormen (2002) halo mass function model since it matches well with halo abundances at high redshift predicted by hydrogen reionization simulations (Zahn et al. 2007). However, the $L(M)$ model introduced in this work can also be combined with other halo mass function models that are calibrated to simulations and observations at lower redshifts. Two-halo terms of the auto/cross-power spectrum can also be

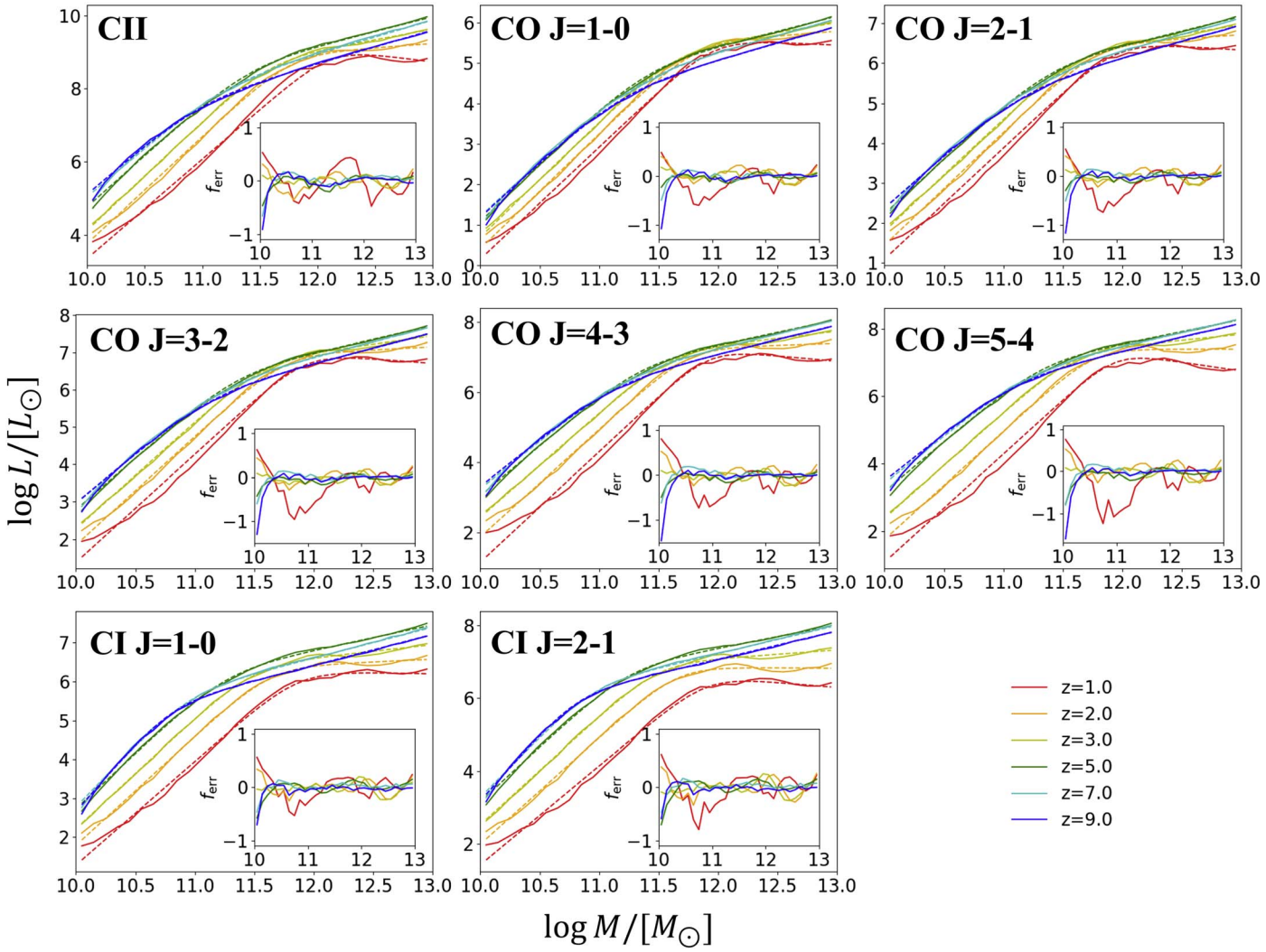

Figure 3. Comparisons of the average value of $L(M)$ between the submillimeter SAM simulation predictions (solid lines) and the double power-law empirical model (dashed lines) at $1 \leqslant z \leqslant 9$. The inset in each panel shows the fractional difference of $L(M)$ relations between submillimeter SAM and the empirical model $f_{\rm err} = (L_{\rm SAM} - L_{\rm model})/L_{\rm SAM}$.

estimated through

$$P_{ij}^{2-\rm halo}(k, z) = I_i(z) I_j(z) \langle b_i(z) \rangle \langle b_j(z) \rangle P_{\rm lin}(k, z), \quad (6)$$

where $P_{\rm lin}$ is the linear theory density power spectrum, i and j are indices for submillimeter lines considered in this work, and $\langle b \rangle$ is the luminosity weighted halo bias,

$$\langle b_i(z) \rangle = \frac{\int dM \frac{dn}{dM} f_{\rm duty} L_i(M, z) b(M, z)}{\int dM \frac{dn}{dM} f_{\rm duty} L_i(M, z)}. \quad (7)$$

In this work we use the halo bias model $b(M)$ proposed by Sheth et al. (2001). At small scales where Poisson noise dominates the power spectrum term, models for the scatter and correlations of $L(M)$ relations become important for the shot-noise power spectrum estimation:

$$P_{ij}^{\rm shot}(z) = \left(\frac{c}{4\pi H(z)}\right)^2 \frac{1}{\nu_i^0 \nu_j^0} \times \int dM \frac{dn}{dM} \langle L_i(M, z) L_j(M, z) \rangle f_{\rm duty}(M, z), \quad (8)$$

where $\langle L_i(M, z) L_j(M, z) \rangle$ denotes the average line i and line j luminosity product of all star-forming halos at a given halo mass at redshift z.

We find that in the submillimeter SAM simulations the luminosity distribution of star-forming halos within a narrow halo mass bin is close to lognormal with a mean given by Equation (1) and a dispersion of σ dex:

$$\frac{dP}{d \log \hat{L}} = \frac{1}{\sigma \sqrt{2\pi}} \exp \times \left[-\frac{1}{2} \left(\frac{\log \hat{L} - \log L + \ln(10) \sigma^2/2}{\sigma} \right)^2 \right]. \quad (9)$$

Here we use $\hat{L}$ to denote the halo luminosities predicted by the submillimeter SAM. L denotes the average halo luminosity given by the model presented in Section 4.1. Note that this approximation only holds if we remove quenched galaxies from our distributions, necessitating the inclusion of the above $f_{\rm duty}$ factor. This differs from previous works that tend to include one or the other of a scattering or duty cycle effect (see, e.g., Keating et al. 2016).

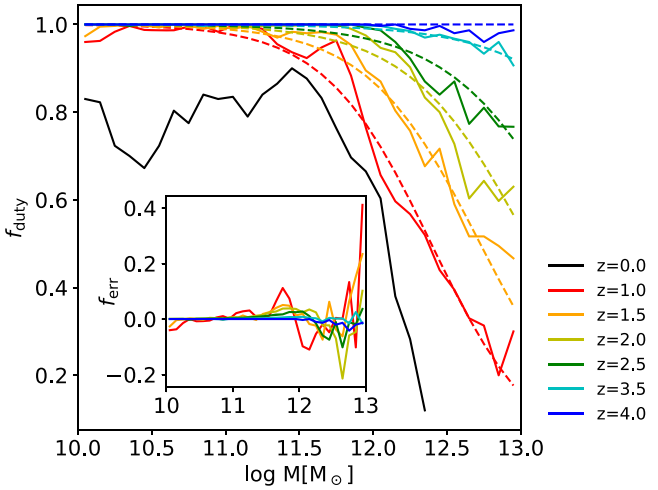

Figure 4. $f_{\rm duty}(M)$ comparisons between SAM simulations and the double power-law empirical model predictions at $1 \leqslant z \leqslant 4$. The solid curves show $L(M)$ relations simulated by SAM + submillimeter SAM, while the dashed lines are given by the empirical model in Equation (3). The inset shows the fractional difference of $f_{\rm duty}(M)$ relations between SAM and the empirical model $f_{\rm err} = (f_{\rm duty}^{\rm SAM} - f_{\rm duty}^{\rm model})/f_{\rm duty}^{\rm SAM}$. At $z < 1$, the SAM $f_{\rm duty}(M)$ relations become more complicated than a double power law owing to low mass halo quenching by stellar feedback, as shown by the black curve.

The average line luminosity product under this assumption on the $L(M)$ distribution is given by

$$\begin{aligned}&\langle L_i(M, z)L_j(M, z)\rangle \\ &= (\rho_{ij}\sqrt{10^{\ln(10)\sigma_i^2} - 1}\sqrt{10^{\ln(10)\sigma_j^2} - 1} + 1)L_i(M, z)L_j(M, z),\end{aligned} \tag{10}$$

where ρ_{ij} is the correlation coefficient between $L_i(M, z)$ and $L_j(M, z)$. Consider the $i = j$ case, where we study the variance of one emission line. In this case, ρ will always be unity and Equation (10) reduces to

$$\langle L_i^2(M, z)\rangle = 10^{\ln(10)\sigma_i^2} L_i^2(M, z). \tag{11}$$

We ignore the halo mass dependence of the dispersion in $L(M)$. Instead of constructing a comprehensive $\sigma(M, z)$ empirical model for the dispersion, we equate the shot-noise power spectrum simulated by the submillimeter SAM to the empirical model prediction and solve for a characteristic $L(M)$ scatter. We summarize the redshift evolution of σ for each submillimeter emission line as follows:

$$\begin{aligned}\sigma_{\rm CII}(z) &= 0.32\exp(-z/1.5) + 0.18,\\ \sigma_{\rm CO}\ J = 1 - 0(z) &= 0.357 - 0.0701z + 0.00621z^2,\\ \sigma_{\rm CO}\ J = 2 - 1(z) &= 0.36 - 0.072z + 0.0064z^2,\\ \sigma_{\rm CO}\ J = 3 - 2(z) &= 0.40 - 0.083z + 0.0070z^2,\\ \sigma_{\rm CO}\ J = 4 - 3(z) &= 0.42 - 0.091z + 0.0079z^2,\\ \sigma_{\rm CO}\ J = 5 - 4(z) &= 0.44 - 0.085z + 0.0063z^2,\\ \sigma_{\rm CI}\ J = 1 - 0(z) &= 0.39 - 0.076z + 0.0063z^2,\\ \sigma_{\rm CI}\ J = 2 - 1(z) &= 0.46 - 0.096z + 0.0079z^2.\end{aligned} \tag{12}$$

We present the $\sigma(z)$ comparisons between submillimeter SAM and Equation (12) for [C II], CO $J = 1$–0, and [C I] $J = 1$–0 in Figure 5.

Assuming a lognormal $L(M)$ distribution, another quantity we need to model is the correlation coefficient ρ. Through studying the correlation among [C II], CO, and [C I] lines

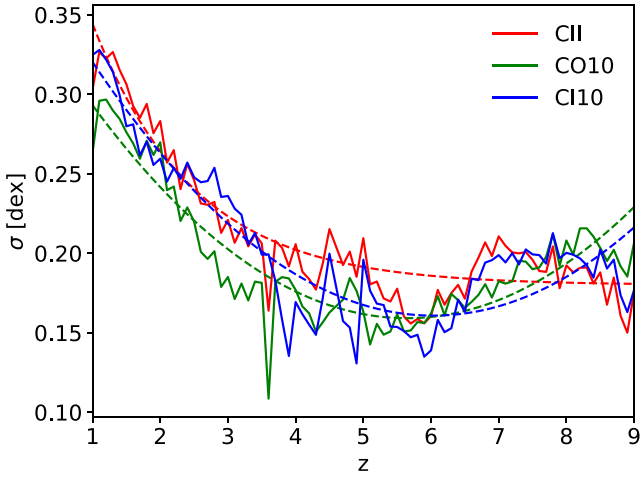

Figure 5. Comparisons of the line emission scatter $\sigma(z)$ between the submillimeter SAM simulation predictions (solid lines) and the model given by Equation (12) (dashed lines) at $1 \leqslant z \leqslant 9$ for [C II] (red), CO $J = 1$–0 (green), and [C I] $J = 1$–0 (blue).

simulated by the submillimeter SAM, we find that the correlation coefficient generally shows weak dependence over $\log(M/[M_\odot]) \lesssim 11$ and $z \lesssim 4$, as presented in the left panel of Figure 6. The CO–[C I] line correlation weakens at high redshift and in the high halo mass range for the following reason: the molecular gas and stellar mass surface density of individual galaxies in this part of parameter space are high owing to rapid gas accretion and relatively weak stellar and AGN feedback. Since the submillimeter SAM assumes the UV radiation field strength to be proportional to the star formation rate surface density, molecular clouds in halos with $\log(M/[M_\odot]) > 11$ and $z > 4$ are subjected to strong UV radiation fields. As a result, a large amount of carbon is singly ionized, leaving limited volume where C I and CO compete with each other. We define the characteristic correlation coefficient ρ_{ij} between two target lines as a value that equates the shot-noise power spectrum given by the SAM and the empirical model:

$$\begin{aligned}&\int d\ln M \frac{dn}{d\ln M}\langle L_i(M, z)L_j(M, z)\rangle f_{\rm duty}\\ &= (\rho_{ij}(z)\sqrt{10^{\ln(10)\sigma_i^2} - 1}\sqrt{10^{\ln(10)\sigma_j^2} - 1} + 1)\\ &\times \int d\ln M \frac{dn}{d\ln M} L_i(M, z)L_j(M, z)f_{\rm duty}.\end{aligned} \tag{13}$$

The resulting cross-correlation ρ factors averaged over all redshift snapshots are presented in the right panel of Figure 6. The characteristic correlation coefficients simulated by the submillimeter SAM are mostly consistent with the empirical galaxy generator (EGG) simulation results (Schaan & White 2021). Despite adopting independent simulation approaches, we find that the correlation coefficients both among CO and among [C I] lines are close to unity. This is a natural prediction because CO lines are all emitted by the CO molecules. The luminosity ratios among CO lines are therefore less sensitive to gas-phase metallicity, external radiation field, and many other environmental variables. The same argument is also applicable to [C I] lines. However, we find that the $\rho_{\rm CO,\ CI}$ factors predicted by the submillimeter SAM are slightly lower compared to the predictions of the EGG simulator, while

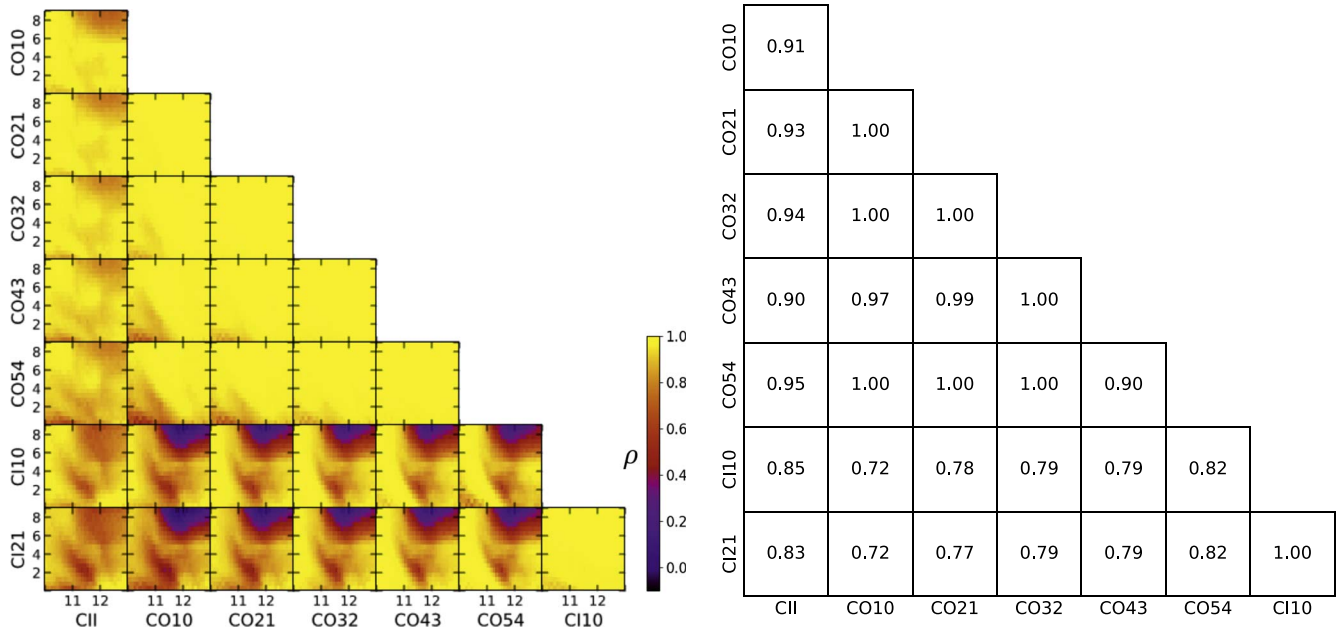

Figure 6. Cross-correlation coefficients ρ among submillimeter emission lines considered in this work. The outer x- and y-axis labels specify the target emission lines. Left: the inner x-axis of each cell shows the halo mass $10 \leqslant \log(M/[M_{\odot}]) \leqslant 13$, divided into 30 log mass bins. The y-axis shows the redshift of the submillimeter SAM simulation output $0 \leqslant z \leqslant 9$, divided into 18 bins. The color map specifies ρ of star-forming halos in the corresponding halo mass and redshift bin. Besides the $\rho_{\mathrm{CO}\times\mathrm{CI}}$ lines at $z \gtrsim 6$ and $\log(M/[M_{\odot}]) \gtrsim 11$, we find that the cross-correlation coefficients show weak mass and redshift dependence. Right: the [C II], CO, and [C I] line cross-correlation coefficients of all the star-forming halos in the submillimeter SAM.

$\rho_{\mathrm{CII,CO}}$ and $\rho_{\mathrm{CII,CI}}$ factors predicted by the submillimeter SAM are significantly higher than EGG's predictions. The $\rho_{\mathrm{CO,\ CI}}$ difference could be caused by the fact that the EGG correlation coefficients are only studied out to redshift $z = 4$, while our work extends to $z = 9$. Note that both the ionized and neutral ISM phases contribute to the [C II] line radiation. The difference among $\rho_{\mathrm{CII,CO}}$ and $\rho_{\mathrm{CII,CI}}$ could be caused by our different assumptions about the molecular cloud masses. If the molecular clouds are assumed to be small, the galaxy star formation activity can ionize the whole cloud such that it becomes [C II] luminous while very faint in CO and [C I] lines. This will lead to small or even negative correlations among [C II], CO, and [C I] lines. On the other hand, if the molecular clouds in a simulation are large enough such that an increase of H II region volume will not significantly influence the molecular gas reservoir, increasing the SFR will boost the strength of all the submillimeter lines considered in this work. In this case we expect [C II], CO, and [C I] lines to be strongly positively correlated, as suggested by the submillimeter SAM. This illustrates the sensitivity of these kinds of predictions to the uncertain details of the assumed subgrid model.

We also compare the $L_{\mathrm{CO}}\,J = 5-4$ versus $L_{\mathrm{CO}}\,J = 2-1$ relation and $L_{\mathrm{CO}}\,J = 5-4/L_{\mathrm{CO}}\,J = 2-1$ ratios predicted by the SAM with observational measurements as a test of the robustness of the correlation predictions. Specifically, we combine the SAM + submillimeter SAM adopted in this work with the 2 deg^2 mock light cone introduced in Yang et al. (2021) to simulate submillimeter line luminosities of star-forming galaxies. We then compare the CO $J = 5$–4 versus CO $J = 2$–1 spectral line energy distribution (SLED) predicted by the SAM with observations at $z \sim 2$ (Valentino et al. 2020). We find that the SAM + submillimeter SAM CO SLED predictions at high [C I] $J = 1$–0 luminosity are in reasonable agreement with the observed $L_{\mathrm{CO}}\,J = 5-4/L_{\mathrm{CO}}\,J = 2-1$ scatter, as shown in Figure 7. Some of the scatter in the observed relation may of course be due to observational errors.

5. Summary Statistic Cross-check between Submillimeter SAM and the Empirical Model

In this section we cross-check the LIM statistics predicted by the submillimeter SAM and the empirical model introduced in Section 4 in order to test how accurately our model represents the SAM simulation results, as judged by commonly used summary statistics.

We first compare the line intensity predictions. Specifically, we combine the $L(M, z)$ and $f_{\mathrm{duty}}(M, z)$ relations given by the submillimeter SAM simulation with the halo model Equation (5) to calculate the submillimeter line intensity predictions. We compute the line intensity predictions of the empirical model in a similar way, using the $L(M, z)$ and $f_{\mathrm{duty}}(M, z)$ relations from Equations (1) and (3) instead of the submillimeter SAM predictions for these quantities. We present the line intensity comparisons in Figure 8. In the redshift range $1 \leqslant z \leqslant 9$, our empirical model predictions agree with the submillimeter SAM simulations to generally better than 10% accuracy. Fractional differences between the submillimeter SAM and this model's predictions jump at $z = 4$ and $z = 5$, as shown in the bottom panel of Figure 8. This is caused by the fact that we fit for parameters in this empirical $L(M, z)$ model in redshift intervals $1 \leqslant z < 4$, $4 \leqslant z < 5$, and $5 \leqslant z \leqslant 9$ (see Table 1), i.e., the $L(M, z)$ model parameters behave discontinuously at $z = 4$ and $z = 5$.

We then check the line emission auto- and cross-power spectra. As mentioned in Section 4, the LIM analyses in this work are all calculated at scales larger than those of dark matter halos, so we will ignore the one-halo term in the power spectrum. For simplicity we also ignore the redshift space distortion. We calculate the power spectrum as

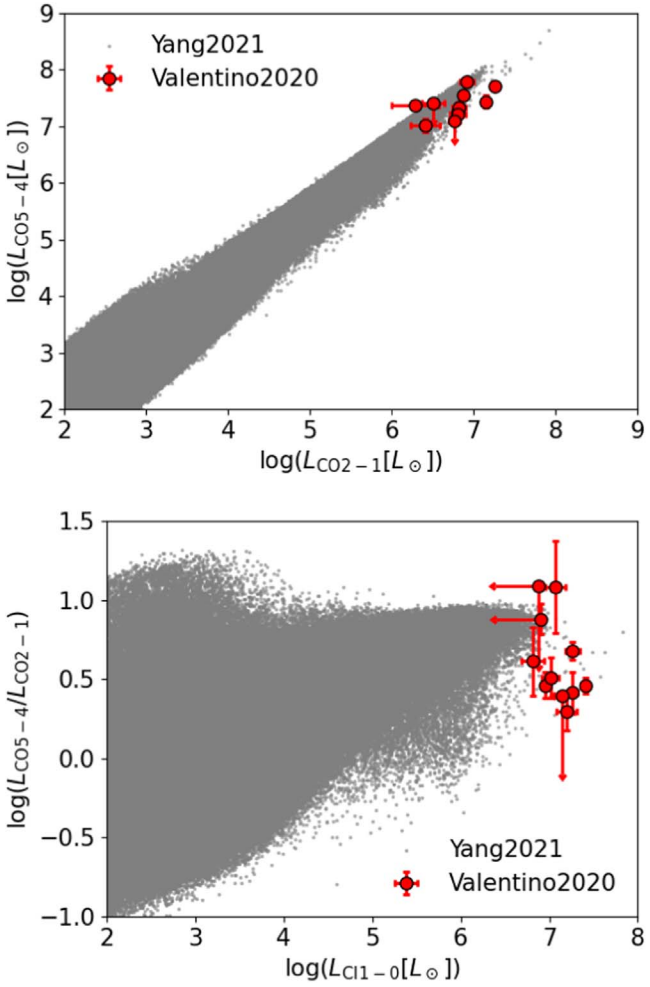

Figure 7. CO SLED comparisons between submillimeter SAM simulations and observations at $1.1 \leqslant z \leqslant 1.3$. Gray points are submillimeter line luminosities of star-forming galaxies predicted by the submillimeter SAM adopted in this work combined with a 2 deg^2 mock light cone introduced in Yang et al. (2021). Red data points are from Table 2 of Valentino et al. (2020). Top: CO $J = 5$–4 vs. CO $J = 2$–1 luminosity relation. Bottom: luminosity ratios between CO $J = 5$–4 and CO $J = 2$–1 line vs. [C I] $J = 1$–0 luminosity.

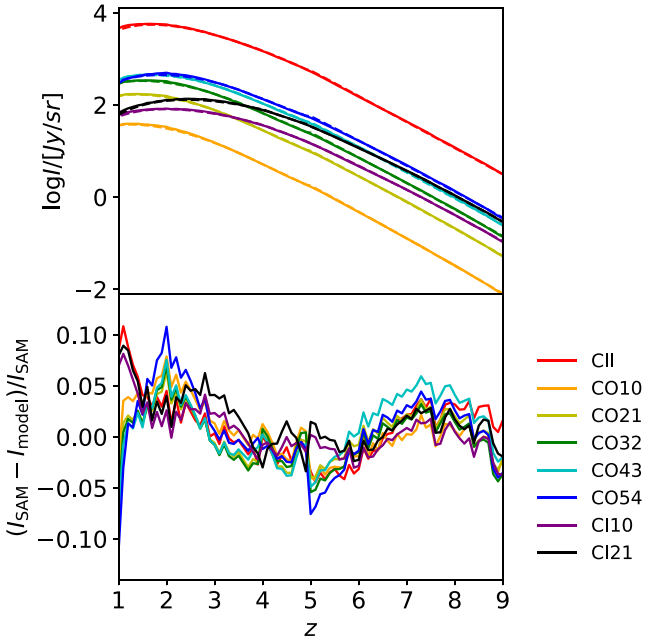

Figure 8. Integrated line intensity comparisons between submillimeter SAM simulations and the empirical model predictions at $1 \leqslant z \leqslant 9$, for various lines as shown in the plot label. Top: the solid curves show line intensities from the submillimeter SAM, while dashed lines are obtained from the empirical models. Bottom: the fractional differences between submillimeter SAM and empirical model predictions for the integrated line intensity.

$P_{ij}(k, z) = P_{ij}^{2-\mathrm{halo}}(k, z) + P_{ij}^{\mathrm{shot}}(z)$, where the two-halo term and the shot-noise term are given by Equations (6) and (8). We use $L(M, z)$, f_{duty}, and $\langle L_i(M, z) L_j(M, z)\rangle$ given by the submillimeter SAM for the simulation power spectra calculations. For the empirical model power spectrum estimation we use the $L(M, z)$, f_{duty}, $L(M)$ scatter, and correlation coefficient models introduced in Section 4. In Figure 9 we show example comparisons between the submillimeter SAM and the empirical model for the auto- and cross-power spectra among the [C II], CO $J = 1$–0, and [C I] $J = 1$–0 lines. We find that the empirical model power spectrum predictions are in agreement with the submillimeter SAM simulations with fractional error less than 25% at $z \geqslant 1$. The SAM model agreement increases to better than 15% at $z \geqslant 3$.

To further test our approach, we also compare with the predictions of a 2 deg^2 mock light cone where halos have been extracted from a dissipationless N-body simulation and filled with galaxies using the submillimeter SAM approach, as described by Yang et al. (2021). In order to assess the differences between the modeling approaches relative to the precision of upcoming LIM experiments, we use as a fiducial example a COMAP-like survey with parameters taken from Li et al. (2016). Specifically, we create LIM mock data in the frequency range $30 \leqslant \nu/[\mathrm{GHz}] \leqslant 34$ with frequency resolution $\Delta\nu = 40$ MHz and angular resolution $\theta_{\mathrm{pix}} = 0.'6$. We then smooth the mock data with a Gaussian beam with FWHM $\theta_{\mathrm{FWHM}} = 6'$ such that the smoothed map spatial resolution matches that of COMAP. We assume a map sensitivity 41.5 μK MHz$^{1/2}$ and estimate the COMAP instrumental noise as a Gaussian probability density distribution with zero mean and standard deviation σ_N, where σ_N is calculated as the map sensitivity multiplied by $10/\sqrt{8\ln(2)\Delta\nu}$. Due to the limited cosmic volume and sensitivity of this mock data, we only compare power spectra predicted by different models in the range $0.1 \leqslant k/[\mathrm{Mpc}^{-1}] \leqslant 0.3$. On smaller scales the mock is dominated by the instrumental noise.

We present the CO $J = 1$–0 power spectra from the submillimeter SAM light cone and the empirical model introduced in this work in Figure 10. We show cases in which the submillimeter SAM power spectrum is computed from all galaxies in the light cone compared with a case where we exclude galaxies in quenched halos (using the same criterion presented in Section 4). We also compare the CO $J = 1$–0 power spectrum using the predictions of submillimeter line luminosities and scatter predicted by the empirical model introduced in Section 4. The error bars show the COMAP 1σ measurement error contributed by the instrumental noise, CO $J = 2$–1, and CO $J = 3$–2 interloper lines. We find that the amplitude decrease of the power spectrum in the submillimeter SAM caused by ignoring quenched halos is much smaller than the measurement error, indicating that the star-forming halos dominate the LIM statistics. This justifies our treatment of quenched halos in the empirical model. The power spectrum predicted by our empirical model has amplitude 8%–12% lower than the submillimeter SAM full COMAP power

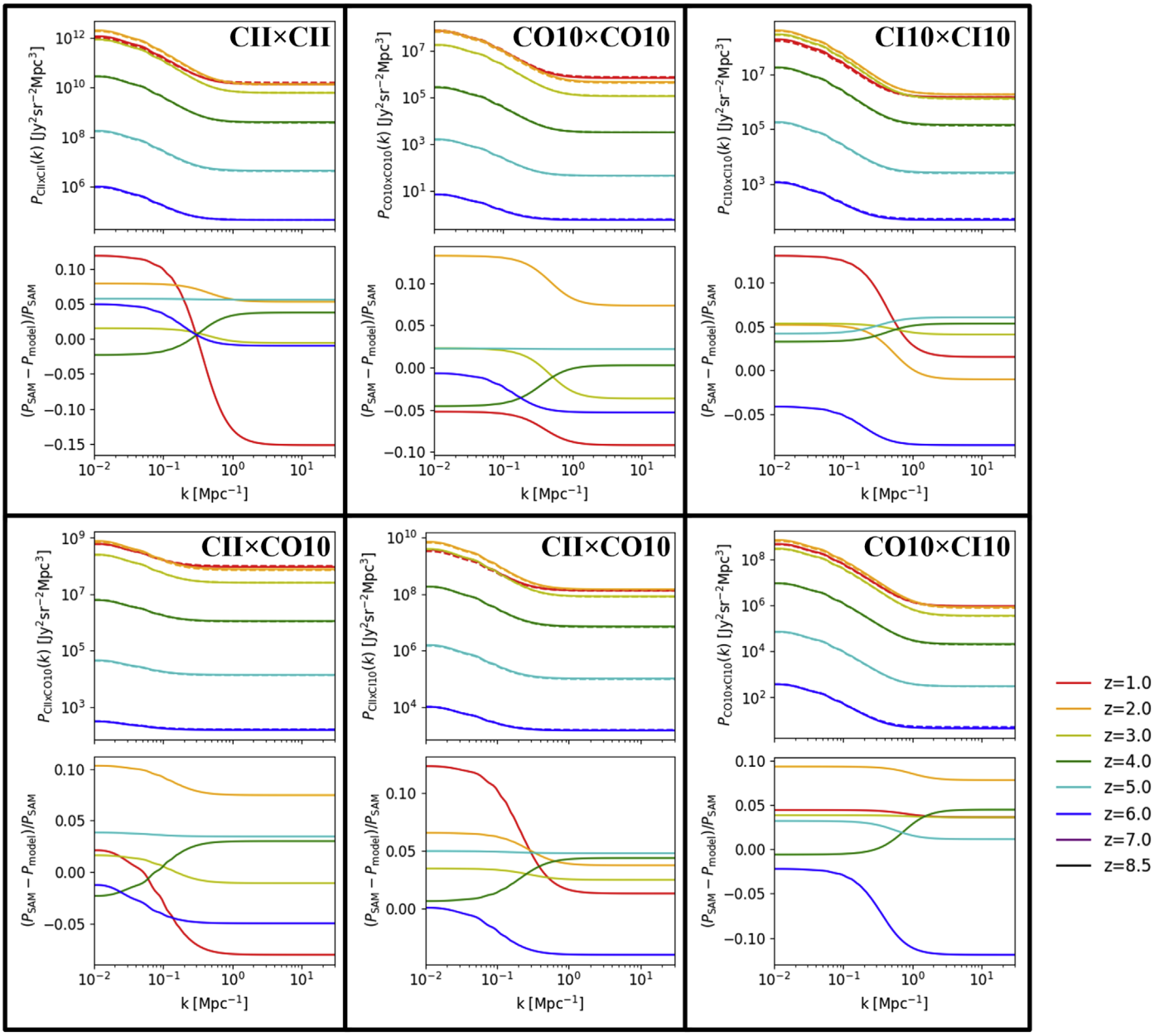

Figure 9. Power spectrum comparisons between submillimeter SAM simulations and the empirical model predictions at $1 \leqslant z \leqslant 9$ among [C II], CO $J = 1$–0, and [C I] $J = 1$–0 lines. The first row shows LIM auto-power spectra, while the bottom row shows the cross-power spectra comparisons. In the upper section of each panel, the solid curves are given by the submillimeter SAM, while dashed lines are predictions of the empirical models. The lower panel shows the power spectrum fractional difference between submillimeter SAM and the empirical model.

spectrum and 3%–7% lower than the SAM star-forming power spectrum. Reduced χ^2 tests show that these three sets of power spectra are indistinguishable considering the measurement error.

6. Discussion and Conclusion

Submillimeter LIM is an emerging observational technique that has the potential to constrain many important features of galaxy evolution and cosmology. Computationally efficient, physically grounded theoretical submillimeter line emission models that accurately capture the strength, scatter, and correlations of multiple lines are crucial for forecasting and interpreting the results of these experiments. In this work, we refine the state-of-the-art multiline submillimeter SAM simulation framework proposed in P19 and construct a simple empirical model calibrated to this physically motivated simulation. Specifically, we model the simulated submillimeter line luminosity versus halo mass relation of star-forming halos as a double power law and provide carefully calibrated models for the halo duty cycle factor, the dispersion in luminosity at fixed halo mass, and the correlations among different submillimeter lines.

We find that our empirical model can reproduce the integrated line intensity and power spectrum of [C II], CO $J = 1$–0 to $J = 5$–4, and [C I] $J = 1$–0 to $J = 2$–1 predicted by the submillimeter SAM simulation with less than 10% and 25% fractional error at $z \geqslant 1$. This model provides a very computationally efficient yet physically grounded approach for CO high-J interloper line removal, molecular hydrogen

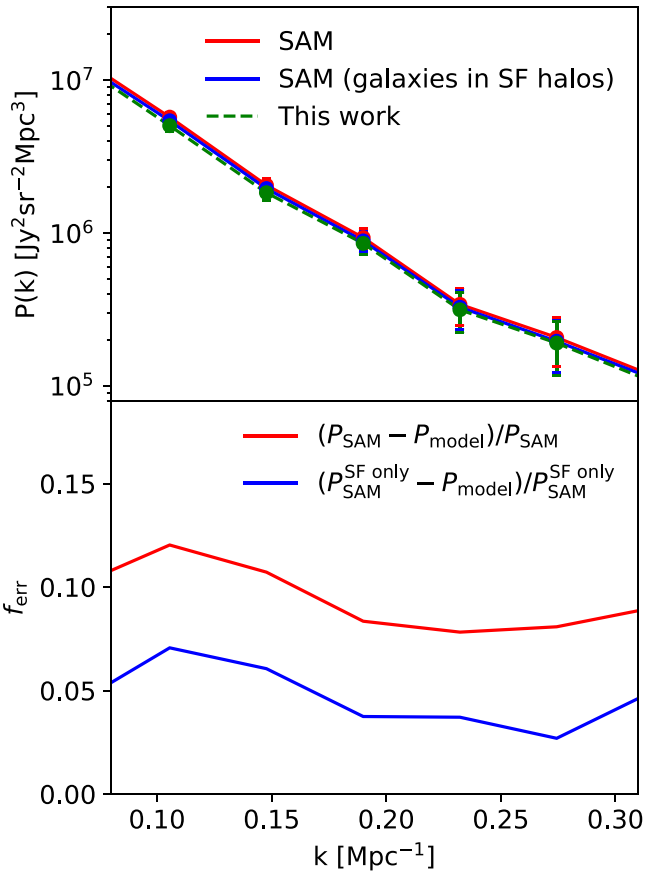

Figure 10. Top: fiducial COMAP CO $J = 1$–0 power spectrum predictions obtained from the submillimeter SAM run within a light cone extracted from a dissipationless N-body simulation, compared with the prediction from the empirical model presented in this work. The red lines show the predictions from the submillimeter SAM light cone including all the simulated galaxies, while the blue lines show the light cone results only including galaxies in star-forming halos. The green dashed line shows the power spectrum predicted by applying the empirical model introduced in this work to the star-forming dark matter halos in the mock light cone. The error bars show 1σ measurement errors typical of the COMAP experiment. Bottom: the red curve shows the CO power spectrum fractional difference between submillimeter SAM and this work. The blue curve shows the fractional difference between CO power spectrum predicted by submillimeter SAM, where only galaxies living in the star-forming halos are considered, and the power spectrum predicted by this work.

density constraints, and other [C II] and CO LIM survey forecasts (Breysse et al. 2021; A. Pullen et al. 2022, in preparation). For applications that may require greater accuracy than that of our current empirical model, we also provide the full tabulated $L(M, z)$, $f_{\rm duty}(M, z)$, and the covariances among [C II], CO, and [C I] lines from the submillimeter SAM predictions at $0 \leqslant z \leqslant 9$ in https://users.flatironinstitute.org/~rsomerville/Data_Release/LIM/.

A careful comparison between the SAM + submillimeter SAM $L(M, z)$ relations and other models (including Righi et al. 2008; Visbal & Loeb 2010; Pullen et al. 2013; Silva et al. 2015; Li et al. 2016; Pullen et al. 2018; Padmanabhan 2019) can be found in Yang et al. (2021, Section 3.2). As discussed in Yang et al. (2021), various $L(M, z)$ models are in reasonable agreement at $11.5 \lesssim \log(M/[M_\odot]) \lesssim 12$ but can be significantly different beyond this halo mass range. This is caused by a lack of submillimeter observational results at very low and high halo masses. The submillimeter line targets selected by galaxy surveys are mainly galaxies with SFR $\sim 10^1$–$10^2[M_\odot\ {\rm yr}^{-1}]$ and halo mass $M \sim 10^{11.5}$–$10^{12}[M_\odot]$. Halos more massive than this range are very rare objects, while galaxies living in halos less massive than this range are generally too faint to be resolved. The upcoming LIM surveys that cover large cosmic volume and faint submillimeter emitter contributions will provide stronger constraints to the shape of $L(M, z)$ relations beyond $11.5 \lesssim \log(M/[M_\odot]) \lesssim 12$. The main advantage of parameterizing $L(M, z)$ relations into a double power law is that we can capture the shape of $L(M, z)$ at very low and high halo masses by parameters α and β, which are sensitive to the strength of stellar feedback and AGN feedback. We leave a study that connects the double power-law $L(M, z)$ relation slopes to various feedback strengths to future works.

The empirical models for these emission lines will be tested by upcoming surveys. For example, preliminary detections of [C II] and CO intensity (Keating et al. 2016; Pullen et al. 2018; Yang et al. 2019) using auto- and cross-power spectra have been used along with priors informed by luminosity functions to constrain empirical models for these lines (Padmanabhan 2018, 2019). Upcoming line intensity mapping surveys will be able to measure power spectra and intensities at much higher precision, which will constrain these models even further. Future works that can connect the parameters in empirical models to physical processes will then be able to measure the physics of galaxies.

We note the major caveats and uncertainties of the models we present here. First, all a priori simulation-based predictions of submillimeter line emission are sensitive to assumptions about the subgrid physics incorporated into the simulation, which govern the physics of star formation, stellar feedback, black hole feedback, etc., shaping the star formation history, gas content, and quenching of galaxies. Significant uncertainties in these physical processes and how to implement them through subgrid prescriptions in cosmological simulations still persist (e.g., Somerville & Davé 2015). Moreover, even for a given set of underlying kiloparsec-scale galaxy properties, the submillimeter line predictions are also sensitive to the assumptions about the properties of the ISM (e.g., the mass distribution and radial profiles of molecular clouds), which are in general not directly resolved in these simulations or in observations except for a few very nearby galaxies. The submillimeter SAM approach used here is no exception, but with the advantage that it is computationally efficient enough to explore the sensitivity to these assumptions, as was done extensively in P19. A further limitation of the P19 approach is that DESPOTIC only computes the line emission from gas in molecular clouds. Some of the observed [C II] emission can also arise from more diffuse cirrus gas, and this is not included in our current models.

We find that the correlation coefficients among CO lines and [C I] lines simulated by the submillimeter SAM framework agree with the EGG simulation results reported in Schaan & White (2021). The value of $\rho_{\rm CO,CI}$ predicted by the submillimeter SAM is slightly lower than EGG's predictions. This is because Schaan & White (2021) only study $\rho_{\rm CO,CI}$ up to $z = 4$, while this work covers a wider redshift range $0 \leqslant z \leqslant 9$. More specifically, at $z \gtrsim 4$, galaxies are more compact and gas-rich and have higher star formation surface density. Since the submillimeter SAM assumes the UV radiation field strength to be proportional to the galaxy star formation rate surface density, carbon atoms in high-redshift molecular clouds tend to

be mostly ionized, leaving limited material that can produce CO and [C I] lines. In this case, CO and [C I] lines can be weakly or even negatively correlated. We also find that $\rho_{\rm CII,CO}$ and $\rho_{\rm CII,CI}$ predicted by the submillimeter SAM are significantly higher than the predictions of the EGG simulator. Considering the fact that the [C II] fine-structure line comes from multiple ISM phases, while CO and [C I] lines are only emitted by dense molecular ISM regions, we believe that this difference may be caused by different assumptions about the molecular cloud properties implemented in the submillimeter SAM and EGG. The limitations on modeling the ionized gas phase in the submillimeter SAM can also lead to biased estimates of the correlation coefficients between [C II] and molecular ISM tracers. Empirically constraining these properties would be a valuable target for future LIM cross-correlation observations. However, the submillimeter SAM does successfully reproduce [C II], CO, and [C I] observational scaling relations at redshift $0 \leqslant z \lesssim 6$, and we emphasize that the simulation results we used for model calibration in this work are consistent with current observations of individual submillimeter sources.

An additional limitation is that we do not attempt to model the correlation of the residuals in the $L(M)$ relations with higher-order halo properties. For example, for stellar masses and star formation rates, it is known that the residual of these quantities from the mean at a given halo mass is correlated with other halo properties, such as formation history (e.g., Matthee et al. 2017), that are known to be correlated with the halo clustering strength via a process called *assembly bias* (Croton et al. 2007). We can think of these as limitations of the standard halo model approach, which could be relatively easily overcome by using SAMs run within merger trees extracted from dissipationless simulations, which we have done in other work (e.g., Gabrielpillai et al. 2021; Hadzhiyska et al. 2021).

Due to the low angular resolution of LIM surveys, interloper lines and continuum foreground contamination, including the Milky Way emission and the cosmic infrared background, are the main challenges for LIM data analysis. Cross-correlating LIM surveys with galaxy surveys that have much higher spatial resolution is one of the best options for removing these contaminants. In this work, we model the aggregate emission of all the galaxies within a halo and do not attempt to separately model central and satellite galaxies or the spatial distribution of satellite galaxies within halos. However, there is no reason in principle that the SAM approach (which also produces predictions for optical properties of individual galaxies) could not be used to develop joint models for traditional galaxy surveys and LIM surveys. We leave this to a future work.

We thank Shenglong Wang for IT support. We thank Dongwoo Chung for useful comments on a draft manuscript. A.R.P. was supported by NASA under award Nos 80NSSC18K1014 and NNH17ZDA001N. R.S.S. is supported by the Simons Foundation. P.C.B. was supported by the James Arthur Postdoctoral Fellowship.

ORCID iDs

Gergö Popping https://orcid.org/0000-0003-1151-4659
Patrick C. Breysse https://orcid.org/0000-0001-8382-5275
Abhishek S. Maniyar https://orcid.org/0000-0002-4617-9320

References

Behroozi, P., Wechsler, R. H., Hearin, A. P., & Conroy, C. 2019, MNRAS, 488, 3143
Behroozi, P. S., Conroy, C., & Wechsler, R. H. 2010, ApJ, 717, 379
Behroozi, P. S., Wechsler, R. H., & Conroy, C. 2013, ApJ, 770, 57
Béthermin, M., Fudamoto, Y., Ginolfi, M., et al. 2020, A&A, 643, A2
Breysse, P. C., Yang, S., Somerville, R. S., et al. 2021, arXiv:2106.14904
Chabrier, G. 2003, PASP, 115, 763
Cooray, A., & Sheth, R. 2002, PhR, 372, 1
Croton, D. J., Gao, L., & White, S. D. M. 2007, MNRAS, 374, 1303
Gabrielpillai, A., Somerville, R. S., Genel, S., et al. 2021, arXiv:2111.03077
Gong, Y., Cooray, A., Silva, M., et al. 2012, ApJ, 745, 49
Hadzhiyska, B., Liu, S., Somerville, R. S., et al. 2021, MNRAS, 508, 698
Helou, G., & Beichman, C. A. 1990, in Liege Int. Astrophysical Colloq. 29, From Ground-Based to Space-Borne Sub-mm Astronomy, ed. B. Kaldeich (Paris: ESA), 117
Kamenetzky, J., Rangwala, N., Glenn, J., Maloney, P. R., & Conley, A. 2014, ApJ, 795, 174
Keating, G. K., Marrone, D. P., Bower, G. C., et al. 2016, ApJ, 830, 34
Keating, G. K., Marrone, D. P., Bower, G. C., & Keenan, R. P. 2020, ApJ, 901, 141
Kovetz, E. D., Viero, M. P., Lidz, A., et al. 2017, arXiv:1709.09066
Krumholz, M. R. 2014, MNRAS, 437, 1662
Lagache, G., Cousin, M., & Chatzikos, M. 2018, A&A, 609, A130
Leung, T. K. D., Olsen, K. P., Somerville, R. S., et al. 2020, ApJ, 905, 102
Li, T. Y., Wechsler, R. H., Devaraj, K., & Church, S. E. 2016, ApJ, 817, 169
Lidz, A., Furlanetto, S. R., Oh, S. P., et al. 2011, ApJ, 741, 70
Madau, P., & Dickinson, M. 2014, ARA&A, 52, 415
Mashian, N., Sturm, E., Sternberg, A., et al. 2015, ApJ, 802, 81
Matthee, J., Schaye, J., Crain, R. A., et al. 2017, MNRAS, 465, 2381
Moriwaki, K., Yoshida, N., Shimizu, I., et al. 2018, MNRAS, 481, L84
Moster, B. P., Naab, T., & White, S. D. M. 2013, MNRAS, 428, 3121
Okamoto, T., Gao, L., & Theuns, T. 2008, MNRAS, 390, 920
Olsen, K., Greve, T. R., Narayanan, D., et al. 2017, ApJ, 846, 105
Olsen, K. P., Burkhart, B., Mac Low, M.-M., et al. 2021, ApJ, 922, 88
Padmanabhan, H. 2018, MNRAS, 475, 1477
Padmanabhan, H. 2019, MNRAS, 488, 3014
Padmanabhan, H., Breysse, P., Lidz, A., & Switzer, E. R. 2021, arXiv:2105.12148
Planck Collaboration, Ade, P. A. R., Aghanim, N., et al. 2016, A&A, 594, A13
Popping, G., Narayanan, D., Somerville, R. S., Faisst, A. L., & Krumholz, M. R. 2019, MNRAS, 482, 4906
Popping, G., Pérez-Beaupuits, J. P., Spaans, M., Trager, S. C., & Somerville, R. S. 2014a, MNRAS, 444, 1301
Popping, G., Somerville, R. S., & Trager, S. C. 2014b, MNRAS, 442, 2398
Popping, G., van Kampen, E., Decarli, R., et al. 2016, MNRAS, 461, 93
Porter, L. A., Somerville, R. S., Primack, J. R., & Johansson, P. H. 2014, MNRAS, 444, 942
Pullen, A. R., Chang, T.-C., Doré, O., & Lidz, A. 2013, ApJ, 768, 15
Pullen, A. R., Serra, P., Chang, T.-C., Doré, O., & Ho, S. 2018, MNRAS, 478, 1911
Righi, M., Hernández-Monteagudo, C., & Sunyaev, R. A. 2008, A&A, 489, 489
Schaan, E., & White, M. 2021, JCAP, 2021, 068
Sheth, R. K., Mo, H. J., & Tormen, G. 2001, MNRAS, 323, 1
Sheth, R. K., & Tormen, G. 2002, MNRAS, 329, 61
Silva, M., Santos, M. G., Cooray, A., & Gong, Y. 2015, ApJ, 806, 209
Somerville, R. S., Barden, M., Rix, H.-W., et al. 2008a, ApJ, 672, 776
Somerville, R. S., & Davé, R. 2015, ARA&A, 53, 31
Somerville, R. S., Gilmore, R. C., Primack, J. R., & Domínguez, A. 2012, MNRAS, 423, 1992
Somerville, R. S., Hopkins, P. F., Cox, T. J., Robertson, B. E., & Hernquist, L. 2008b, MNRAS, 391, 481
Somerville, R. S., & Kolatt, T. S. 1999, MNRAS, 305, 1
Somerville, R. S., Olsen, C., Yung, L. Y. A., et al. 2021, MNRAS, 502, 4858
Somerville, R. S., Popping, G., & Trager, S. C. 2015, MNRAS, 453, 4337
Somerville, R. S., & Primack, J. R. 1999, MNRAS, 310, 1087
Sun, G., Hensley, B. S., Chang, T.-C., Doré, O., & Serra, P. 2019, ApJ, 887, 142
Valentino, F., Magdis, G. E., Daddi, E., et al. 2020, ApJ, 890, 24
Visbal, E., & Loeb, A. 2010, JCAP, 2010, 016
Yang, S., & Lidz, A. 2020, MNRAS, 499, 3417
Yang, S., Pullen, A. R., & Switzer, E. R. 2019, MNRAS, 489, L53
Yang, S., Somerville, R. S., Pullen, A. R., et al. 2021, ApJ, 911, 132

Yang, X., Mo, H. J., van den Bosch, F. C., Zhang, Y., & Han, J. 2012, ApJ, 752, 41
Yung, L. Y. A., Somerville, R. S., Finkelstein, S. L., et al. 2020a, MNRAS, 496, 4574
Yung, L. Y. A., Somerville, R. S., Finkelstein, S. L., Popping, G., & Davé, R. 2019a, MNRAS, 483, 2983
Yung, L. Y. A., Somerville, R. S., Popping, G., et al. 2019b, MNRAS, 490, 2855
Yung, L. Y. A., Somerville, R. S., Popping, G., & Finkelstein, S. L. 2020b, MNRAS, 494, 1002
Zahn, O., Lidz, A., McQuinn, M., et al. 2007, ApJ, 654, 12